Rock and Soil Mechanics

Volume 43 | Issue 10 Article 2

11-25-2022

Experimental research on fracture initiation pressure of conventional triaxial slurry fracturing in similar material of sandy mudstone

Hua CHENG
Anhui Province Key Laboratory of Building Structure and Underground Engineering, Anhui Jianzhu University, Hefei, Anhui 230601, China

Xiang-yang LIU
Anhui Province Key Laboratory of Building Structure and Underground Engineering, Anhui Jianzhu University, Hefei, Anhui 230601, China, lxymm9632@163.com

Ru-kang CAO
School of Civil Engineering and Architecture, Anhui University of Science and Technology, Huainan, Anhui 232001, China

Xue-song WANG
School of Civil Engineering and Architecture, Anhui University of Science and Technology, Huainan, Anhui 232001, China

Custom Citation

CHENG Hua, LIU Xiang-yang, CAO Ru-kang, WANG Xue-song, . Experimental research on fracture initiation pressure of conventional triaxial slurry fracturing in similar material of sandy mudstone[J]. Rock and Soil Mechanics, 2022, 43(10): 2655-2664.

Rock and Soil Mechanics 2022 43(10): 2655−2664 ISSN 1000−7598
https: //doi.org/10.16285/j.rsm.2021.7042 rocksoilmech.researchcommons.org/journal

Experimental research on fracture initiation pressure of conventional triaxial slurry fracturing in similar material of sandy mudstone

CHENG Hua[1, 2, 3], LIU Xiang-yang[1, 3], CAO Ru-kang[1], WANG Xue-song[1]

1. School of Civil Engineering and Architecture, Anhui University of Science and Technology, Huainan, Anhui 232001, China
2. School of Resources and Environmental Engineering, Anhui University, Hefei, Anhui 230601, China
3. Anhui Province Key Laboratory of Building Structure and Underground Engineering, Anhui Jianzhu University, Hefei, Anhui 230601, China

Abstract: To further explore the fracture initiation mechanism of fracture grouting in typical sandy mudstone from Huainan and Huaibei mining areas in China, a conventional triaxial fracture grouting test device was developed, and the model test of fracture initiation pressure of slurry fracturing in similar material of sandy mudstone was carried out. Based on the test results, the influences of rock strength and stress state on grouting fracture initiation pressure and fracture propagation pattern were analyzed, and the fracture initiation mechanism of fracture grouting in sandy mudstone was revealed. The results show that there is a positive correlation between the initiation pressure and the compressive strength of rock; the larger the compressive strength of the rock is, the more complex the fracturing path is. The sensitivity of fracture initiation pressure to confining pressure is much greater than that of axial pressure; the larger the stress difference $\Delta\sigma=\sigma_V-\sigma_H$ is, the more regular the fracture shape is. Under the triaxial condition of pore pressure, the rock tensile strength determined by slurry fracturing method in sealed open hole section is approximately 2.5 times the uniaxial tensile strength. The research results can provide a reference for the design and construction of fracture grouting in similar rock strata in the future.

Keywords: sandy mudstone; conventional triaxial test; fracture grouting; fracture initiation pressure; model test

1 Introduction

In mine engineering, grouting is one of the important construction measures to plug groundwater and reinforce soft rock strata[1−3]. However, with the continuous increase in mining depth in China, the structure of the rock mass becomes diverse and the discontinuities are well developed[4−5], thus resulting in unsatisfactory grouting effect. Since the deep rock strata are characterized by high in situ stress, high water pressure and poor injectability[6], high-pressure fracture grouting is often used in practice to ensure the grouting effect.

The fracture grouting in deep rock strata is a very complex physical process. Numerous scholars have paid their attention to the fracture initiation pattern and the fracture propagation law in the open hole section. Theoretically, Huang[7] stated that the formation of fractures is dominated by the stress state near the hole wall, and proposed the initiation criteria for vertical and horizontal fractures. Chen et al.[8] deduced the stress expression around the inclined open hole section through coordinate transformation, and proposed the discriminant condition of fracturing in the inclined open hole section. Hubbert et al.[9] proposed the theory of tensile failure induced by stress concentration in the hole wall, which is still widely used currently. This theory converts the effects of hydraulic and in situ stresses in the open hole section on the rock mass of the hole wall into the circumferential tensile stress. With the increase in pressure inside the open hole, the circumferential tensile stress will cause tensile failure near the hole wall. However, through pore pressure cracking test on granite and marble, Wu et al.[10] found that the measured fracture initiation pressure in the open hole section is significantly greater than the theoretical value. Therefore, due to cognitive limitations, simple theoretical analysis, at present, cannot fully explain the fracture initiation and propagation mechanism in the open hole section. Yun et al.[11] carried out fracture grouting tests on different sand samples and proposed a prediction model for fracture initiation pressure. Through experiments, Fisher et al.[12] studied the initiation pressure and fracture morphology in the open hole section. Alfaro et al.[13] investigated the fracture initiation in the open hole section through laboratory tests and analyzed the influence of fracture initiation direction on initiation pressure. By means of the electro-hydraulic servo-controlled rock mechanics

Received: 6 December 2021 Revised: 16 June 2022
This work was supported by the National Natural Science Foundation of China (51874005, 51674006, 51878005).
First author: CHENG Hua, male, born in 1956, PhD, Professor, mainly engaged in the teaching and research of underground engineering. E-mail: hcheng@aust.edu.cn
Corresponding author: LIU Xiang-yang, male, born in 1991, PhD, mainly engaged in the research of grouting and water plugging and reinforcement in underground engineering. E-mail: lxymm9632@163.com

test system MTS815, Lin et al.[14] carried out quasi triaxial hydraulic fracturing tests on briquette specimens and raw coal specimens, and found that the formation stress state is the dominant factor affecting the fracturing direction in the open hole section. To sum up, model test is currently the most mature and effective method to understand the mechanism of fracture initiation and propagation in the open hole section.

This study focuses on the typical sandy mudstone in Huainan and Huaibei mining areas. A conventional triaxial fracture grouting test device is developed, and the similar material of sandy mudstone is prepared. Based on the results of triaxial fracture grouting model test, the influences of rock strength and stress state on fracture propagation morphology, fracture grouting initiation pressure, and fracture initiation mechanism are analyzed. The relationship between the fracture grouting tensile strength and the uniaxial tensile strength of the sealed open hole section is discussed by comparing the experimental and theoretical results. This research can provide a reference for the design and construction of fracture grouting in similar rock strata.

2 Similar material modeling test

2.1 Lithology

The sandy mudstone used in this study was sampled from the Permian Upper Shihezi Formation at 431.8 m depth of Matoumen, west ventilating shaft, Yuandian No. 2 Mine, Huaibei, Anhui Province, China[15]. The mudstone was polished and processed into cubic specimens with side length of 100 mm for compression test and tension test. The basic mechanical parameters of the sandy mudstone are listed in Table 1, and the stress-strain curves are shown in Fig. 1.

2.2 Similar materials

In the current tests of rock-like materials, gypsum mixture has become the first choice due to its similar mechanical properties with rock and wide adjustment range of strength and elastic modulus[16−18]. In view of the advantages of gypsum mixture, the similar materials selected in this test are ordinary Portland cement P.O.42.5, quartz sand (through 1.25 mm sieve), ordinary gypsum and water.

Table 1 Mechanical parameters of sandy mudstone

Elastic modulus /GPa	Compressive strength /MPa	Tensile strength /MPa
5.79−6.83	37.42−41.11	2.38−2.93

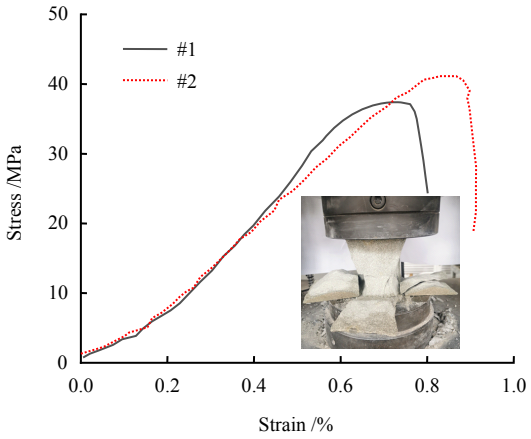

Fig. 1 Stress−strain curves of sandy mudstone

After repetitive trials and referring to Huang et al.[18], the mixing ratio of cement, gypsum and quartz sand was determined to be 7∶3∶3 and 9∶1∶3. A mold with a size of 100 mm×100 mm×100 mm was used to fabricate the specimens for compression test and tension test. To avoid testing errors caused by individual difference of specimens, three compression tests and three tension tests were respectively carried out for specimens with different mixing ratios.

The stress-strain curves obtained from the compression tests are presented in Figs. 2 and 3. By comparing Figs. 1−3, one can see that the mechanical properties of similar materials are close to those of sandy mudstone in field. In addition, the results of three compression tests with the same mixing ratio are basically identical, indicating an acceptable dispersion for specimens with the same mixing ratio. Table 2 lists the compression test results[19]. The elastic modulus E is estimated according to the secant modulus between 70% peak value and 30% peak value at the elastic deformation stage, and the fracture toughness K_{IC} is calculated according to the empirical formula $K_{IC}=\sigma_t/8.23$[20].

By comparing the test results of sampled sandy mudstone and similar materials, it is found that the physical parameters of the specimens are close to the sandstones, which can be used as the similar materials in the following modeling tests.

2.3 Similarity criterion

The sandy mudstone sampled on site has several deficiencies such as irregular shape, well-developed original cracks and severe weathering, thus it is difficult to obtain large-size samples. Therefore, the specimens were poured using rock-like materials, and the model tests were designed according to the similarity criterion. The model should meet the conditions of geometric similarity, stress-strain similarity and strength similarity[21]. From theoretical derivation, the following similarity indices of fracture grouting model test are obtained:

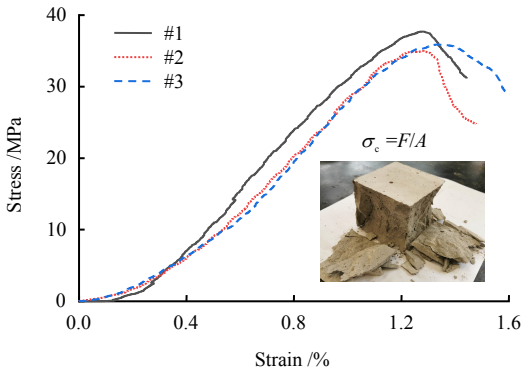

Fig. 2 Stress−strain curves of the first type specimen

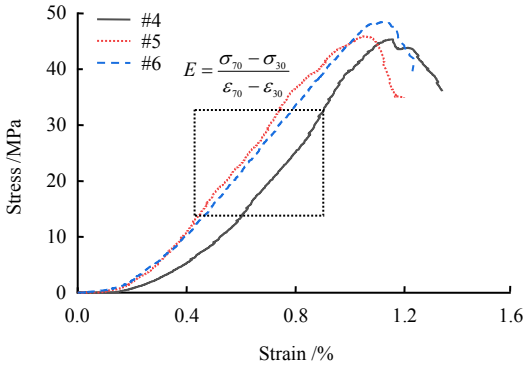

Fig. 3 Stress−strain curves of the second type specimen

Table 2 Compression and tension test results[19]

Cement: gypsum: quartz sand	Specimen No.	Compressive strength σ_c /MPa		Elastic modulus E/GPa		Specimen No.	Tensile strength σ_t /MPa		Fracture toughness K_{IC} /(MPa • m$^{1/2}$)	
		Test value	Mean value	Test value	Mean value		Test value	Mean value	Test value	Mean value
	#1	34.98		4.38		7#	2.63		0.319	
7: 3: 3	#2	35.89	36.19	3.82	4.30	8#	2.65	2.58	0.322	0.313
	#3	37.71		4.71		9#	2.46		0.299	
	#4	45.36		6.39		10#	3.32		0.403	
9: 1: 3	#5	45.86	45.56	6.32	6.32	11#	2.93	3.13	0.356	0.381
	#6	48.47		6.25		12#	3.15		0.383	

$$C_\varepsilon C_l / C_\delta = 1,\ C_E C_\varepsilon / C_\sigma = 1$$
$$C_P / C_\sigma = 1,\ C_{K_{IC}} / C_{\sigma_t} = 1,\ C_\varepsilon = 1 \quad (1)$$

where C_l is the geometric similarity constant; C_P is the load similarity constant; C_ε is the strain similarity constant; C_σ is the stress similarity constant; C_δ is the displacement similarity constant; C_E is the similarity constant of elastic modulus; C_{σ_t} is the similarity constant of tensile strength; and $C_{K_{IC}}$ is the similarity constant of fracture toughness.

The similarity condition of rock-like materials is

$$C_P = C_E = C_\sigma = C_\varepsilon = C_{\sigma_t} = C_{K_{IC}} = 1 \quad (2)$$

2.4 Model test apparatus

The model test was carried out using the self-developed three-dimensional (3D) rock fracture grouting modeling system, as shown in Fig. 4.

The triaxial loading system is composed of an electro-hydraulic servo-controlled pressure testing machine YAW3000 and a high-pressure oil pump YBZ50, which can respectively provide the maximum axial pressure of 30 MPa and the maximum confining pressure of 10 MPa. Two loading paths do not interfere with each other. The inside of the triaxial pressurized chamber is a cylindrical space with a diameter of 380 mm and a height of 380 mm to accommodate cylindrical specimens with a diameter of 350 mm and a height of 350 mm. During the test, the high-pressure oil pump is used to provide pressure for the slurry isolator, which can inject

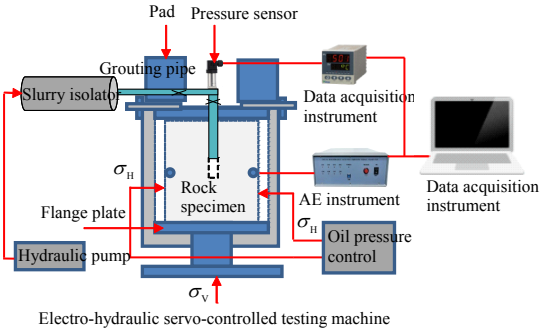

(a) Structure of test apparatus

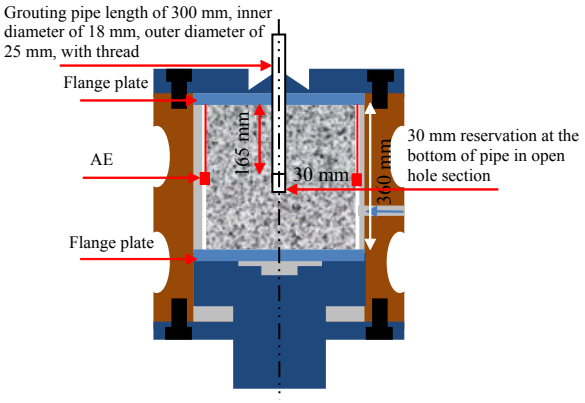

(b) Structure of triaxial pressurized chamber

Fig. 4 Schematic diagrams of test device

the slurry into the open hole section of the specimen. A hydraulic pump is used to control the valve to adjust the grouting pressure until the specimen is cracked, and the peak pressure is taken as the fracture initiation

pressure of the specimen. A flat film pressure sensor, with a range of 0−40 MPa, is employed for real-time pressure monitoring at the orifice of the grouting pipe. The high performance 8-channel acoustic emission (AE) monitoring system DS5-8A is adopted to capture the rock fracture signals during the grouting, so as to monitor the real-time changes of AE energy. The parameter settings are listed in Table 3.

Table 3 Parameter settings of AE device

Number of acquisition channels	Sampling frequency /MHz	Channel data extraction threshold /dB	Gain amplitude of preamplifier /dB
4	3	30	60

2.5 Test schemes

Previous studies have shown that without considering the percolation effect of the open hole section, rock fracture grouting is controlled by the strength and stress state of the injected strata, rather than the properties of the slurry[8]. Therefore, the ordinary cement slurry with water-cement ratio equal to 1 is selected in this study. Since the circumferential pressure is exerted by a hydraulic pump, it is necessary to keep the axial pressure greater than the circumferential pressure to seal the hydraulic pressure. The test schemes of fracture grouting model are listed in Table 4.

Table 4 Test schemes for fracture grouting model

Test No.	Axial stress σ_V /MPa	Circumferential stress σ_H /MPa	Cement: gypsum: quartz sand
#1	0	0	7:3:3
#2	0	0	9:1:3
#3	6	5	7:3:3
#4	6	3	7:3:3
#5	6	1	7:3:3
#6	8	3	7:3:3
#7	4	3	7:3:3

Two material strengths are taken into account in the experiment to explore the influence of different rock strengths on fracture initiation pressure. The stress state is the key factor affecting the fracture initiation pressure in deep rock strata. The axial pressure is controlled by the servo testing machine to model the vertical in situ stress σ_V, and the horizontal in situ stress σ_H is modeled by pumping the hydraulic oil into the pressure chamber through a high-pressure oil pump.

The epoxy resin is applied to the processed specimens to prevent oil infiltration when the confining pressure is loaded. The uniformly-spaced AE probes are installed around the specimen. Butter is smeared on the upper and lower surfaces of the specimen, and rubber pads and flanges are covered to ensure uniform forces on the specimen during the loading test and to meet the sealing requirements, as shown in Fig. 5. After the test, the real-time data recorded by the pressure sensors and AE probes are saved and analyzed, and the fracture propagation morphology is observed.

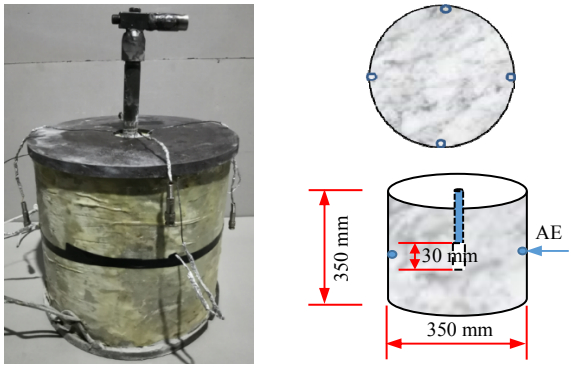

(a) Photo (b) Schematic diagram

Fig. 5 Installation of AE probe

3 Test results and analysis

3.1 Effect of rock strength

3.1.1 AE energy and grouting pressure

Specimens #1 and #2 are subject to the stress state without axial pressure and confining pressure. Therefore, the tests #1 and #2 are conducted outside the triaxial pressure chamber to explore the influence of rock strength on fracture initiation pressure.

As shown in Fig. 6, at the initial stage of grouting, the grouting pressure of specimen #1 remains stable as the slurry is filling the pipe. From 50 s to 150 s, the AE energy does not increase obviously, and the pressure slowly rises to 2.1 MPa, at which point the specimen #1 is at the stage of void compaction. At 150 s, with the rapid rise of grouting pressure, AE energy fluctuates drastically, resulting in pressure suppression. At 180 s, the maximum energy reaches up to 0.24 V • S, with the maximum pressure approaching 6.75 MPa, and then the specimen fails. Then the pressure curve drops rapidly and the AE energy flattens out. In the whole test, the AE energy of specimen #1 is in a good agreement with the grouting pressure curve, indicating that AE signals can effectively monitor the fracture propagation.

In comparison, the fracture initiation pressure of specimen #2 is 8.92 MPa, 2.17 MPa larger than that of specimen #1, indicating that the initiation pressure is positively correlated with the cement content. By comparing the AE energy of specimens #1 and #2, it is found that the AE energy curve of specimen #1 is relatively dense before failure, while the peak energy

of specimen #2 is larger when it is broken. The analysis suggests that the larger the rock strength is, the denser its interior structure is, the shorter the time domain of AE signal generation is, and the sparser the energy curve is. However, larger rock strength also leads to more intense fracture and higher signal peak.

3.1.2 Fracture propagation morphology

Figure 6 displays the side views and fracture profiles of specimens #1 and #2 after fracture grouting. It is clear that there is a crack perpendicular to the transverse direction of the grouting pipe in both specimens. The analysis shows that without external pressure, slurry in the open hole is continuously pressurized, and accumulates energy, leading to the generation of a transverse crack in the shortest direction along the fracture path. By comparing the fracture profiles, it is found that specimen #2 is slightly rough, and there are local twists and turns during crack propagation from the open hole section to the boundary. It can be concluded that the larger the rock strength is, the greater the grouting pressure required for specimen fracturing is. At such a high pressure, slurry is more likely to diffuse through a weak structure plane, forming a complex fracturing path.

3.2 Effect of stress state

3.2.1 AE energy and grouting pressure curve

Under constant axial pressure (6 MPa), the fracture initiation pressures of specimens #3, #4 and #5 corresponding to confining pressures of 5 MPa, 3 MPa and 1 MPa are 16.29 MPa, 11.93 MPa and 8.31 MPa, respectively, and the corresponding AE energy signals increase successively with a large difference. This is because when the axial pressure remains unchanged, with the decrease of confining pressure, the constraining forces of the specimens weaken, which leads to the reduction of the resistance to fracture initiation in the open hole section and the reduction of grouting pressure required for fracturing. Moreover, as the decrease of the compression due to diminished confining pressure, greater energy is released during fracture grouting.

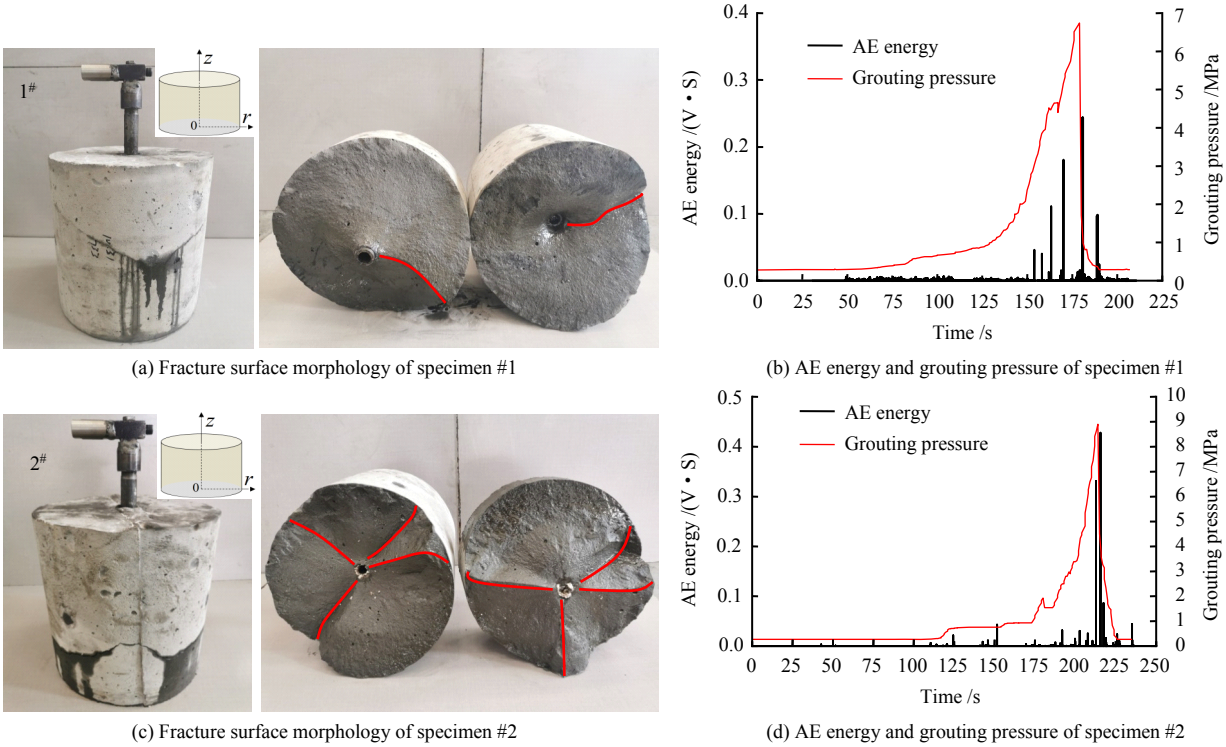

(a) Fracture surface morphology of specimen #1

(b) AE energy and grouting pressure of specimen #1

(c) Fracture surface morphology of specimen #2

(d) AE energy and grouting pressure of specimen #2

Fig. 6 Cross-section morphology and corresponding diagram of AE energy and grouting pressure of specimens #1 and #2 after fracturing

When the confining pressure is constant at 3 MPa, fracture initiation pressures of specimens #6, #4 and #7 corresponding to axial pressures of 8 MPa, 6 MPa and 4 MPa are close to each other, which are 11.18 MPa, 11.93 MPa and 10.51 MPa, respectively, and the corresponding AE energy signals are similar as well. When the axial pressure exceeds the confining pressure, the specimen mainly cracks along the direction perpendicular to the minor principal stress. Since the confining pressure determines the fracture initiation pressure, the initiation pressures of different specimens fall in a small range, and the influence of axial pressure on AE energy signal is insensitive.

The grouting pressure curves measured in the triaxial chamber present two obvious peaks, and the reasons are described as follows: The pressure drops

sharply after specimen failure, thus the first peak corresponds to the fracture initiation pressure. The second peak appears after the specimen fracture, and the grouting pressure is connected with the confining pressure, meaning that the two pressure systems are neutralized without falling to zero. Then the slurry continues to be injected, leading to the pressure rising again, and the pressure drops rapidly after unloading the confining pressure.

3.2.2 Morphological characteristics of fracture propagation

In Fig. 7, for specimen #3, the angle between the fracture and the *z*-axis is approximately 30° and the fracture extends to the upper and lower surfaces, but the area near the open hole section presents a relatively flat vertical fracture initiation surface. The fracture of specimen #4 transitions from parallel to *z*-axis to L-shaped fracture perpendicular to *z*-axis, and the area near the open hole section also presents a relatively flat vertical fracture initiation surface. The splitting crack of specimen #5 is parallel to *z*-axis and penetrates the upper and lower surfaces of the specimen. To sum up, during the test, the axial pressures of these three specimens are constant. The higher the confining pressure is, the severer the circumferential constraint is, the greater the resistance to be overcome for crack initiation around the open hole is, and the more complex the fracture morphology is. On the contrary, a small confining pressure means that there is little resistance for crack initiation in the open hole section, and it is easy to crack along the direction parallel to the major principal stress (*z*-axis).

As shown Fig. 7, the fracture surface of specimen #6 is parallel to *z*-axis and penetrates through the upper and lower surfaces. The fracture surface of specimen #7 changes from transverse fracture perpendicular to *z*-axis to about 45° with respect to *z*-axis, and the fracture surface is relatively smooth. By comparing the fracture surface morphology of specimens #6, #4 and #7, it is observed that the fracture propagation paths become regular with the increase of axial pressure when the confining pressure is constant.

Comparing specimens #3−#7, it is found that the stress difference ($\Delta\sigma = \sigma_{\mathrm{V}} - \sigma_{\mathrm{H}}$) has a significant effect on the morphology of fracture surface. The fracture morphology tends to be regular with the increase of stress difference, and the direction of fracture initiation is gradually perpendicular to the direction of minor principal stress. With the decrease of stress difference and uneven distribution of axial compression, the three directions of the principal stresses deviate, and the formed fracture turns to or away from the *z*-axis.

4 Comparative analysis between test and theoretical calculation

If the rock strata are in a completely elastic state, the vertical stress mainly comes from the overburden[22], which increases linearly with the depth, and can be expressed as

$$\sigma_{\mathrm{V}} = \sum_{i=1}^{n} \gamma_i H_i \tag{3}$$

where γ_i is the unit weight of rock strata; and H_i is the height of each rock layer.

The horizontal stress is mainly induced by horizontal tectonic movement and vertical stress, and it also linearly increases with the depth, which can be calculated according to the principle of rock mechanics:

$$\left.\begin{aligned} \sigma_{\mathrm{H}} &= k_1\sigma_{\mathrm{V}} + P_{\mathrm{S}} \\ \sigma_{\mathrm{h}} &= k_2\sigma_{\mathrm{V}} + P_{\mathrm{S}} \end{aligned}\right\} \tag{4}$$

where σ_{h} is the horizontal minor principal stress; P_{S} is the pore pressure[23]; and k_1 and k_2 are the lateral pressure coefficients in both directions on horizontal plane.

Figure 8 illustrates the forces on the open hole fracture. Following assumptions are made based on the analysis above: (1) the azimuth of the open hole section is consistent with the three directions of the principal stresses of rock strata, and its cross-section is parallel to the horizontal principal stress; (2) the rock strata are completely elastic; and (3) the slurry loss does not occur in the open hole.

When the vertical principal stress σ_{V} is the minimum, we can know from Fig. 8(a) that the total stress σ_z in the vertical direction in the open hole section is

$$\sigma_z = P - \sigma_{\mathrm{V}} \tag{5}$$

where *P* is the grouting pressure in the open hole section.

According to the maximum tensile stress failure criterion, brittle tensile fracture occurs when the vertical stress reaches the rock tensile strength, i.e. the fracturing condition can be expressed as $\sigma_z = \sigma_{\mathrm{t}}$. The grouting pressure is the same as the fracture pressure at this time. If no slurry loss occurs in the open hole section, the transverse fracturing should meet the following condition:

$$P = \sigma_{\mathrm{t}} + \sigma_{\mathrm{V}} \tag{6}$$

In this case, the grouting pressure in the open hole section counteracts the effect of the longitudinal load and the fracture toughness of the rock itself, thus causing transverse fracture initiation.

When the minor horizontal principal stress σ_{h} is the minimum, it can be seen from Fig. 8(c) that the radial stress σ_ρ, tangential stress σ_θ and shear stress $\tau_{r\theta}$ of the open hole section under horizontal principal stress can be calculated as follows[24]:

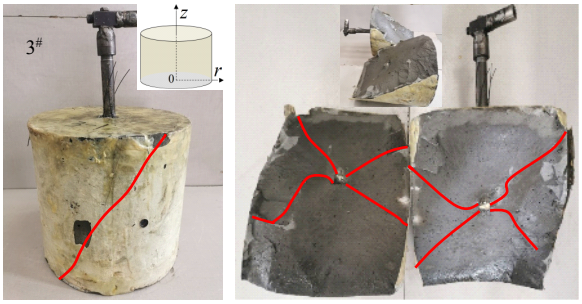

(a) Fracture surface morphology of specimen #3

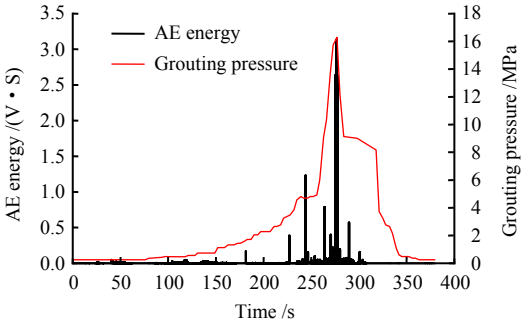

(b) AE energy and grouting pressure of specimen #3

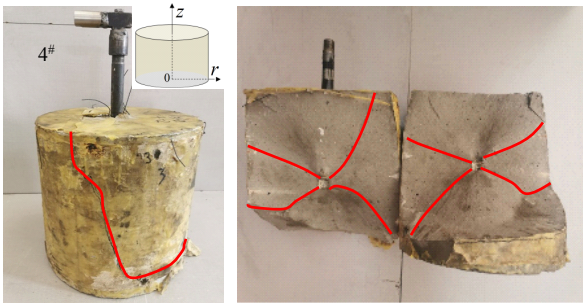

(c) Fracture surface morphology of specimen #4

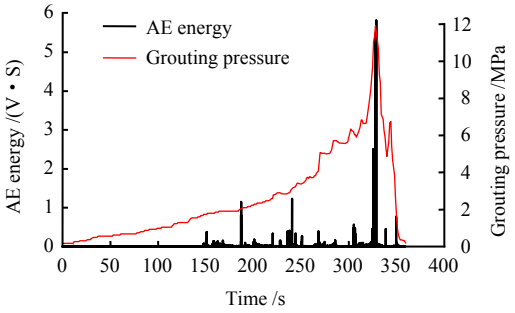

(d) AE energy and grouting pressure of specimen #4

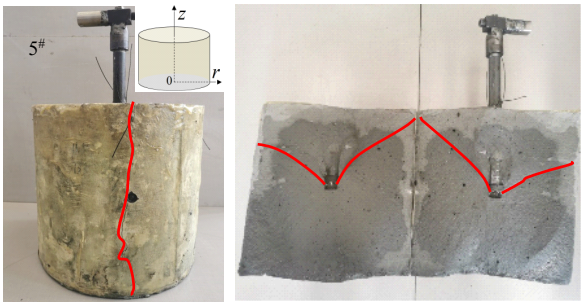

(e) Fracture surface morphology of specimen #5

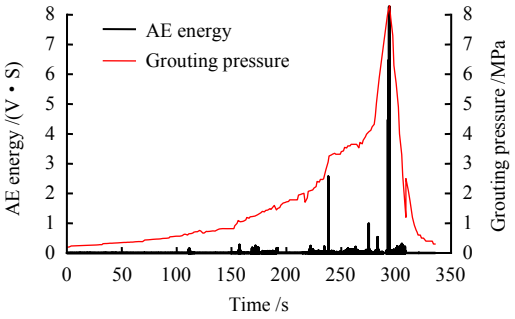

(f) AE energy and grouting pressure of specimen #5

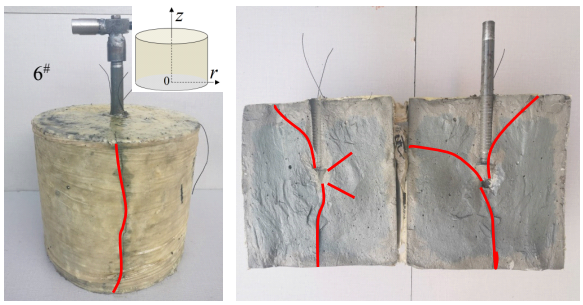

(g) Fracture surface morphology of specimen #6

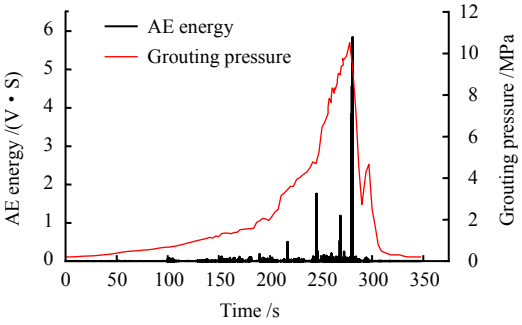

(h) AE energy and grouting pressure of specimen #6

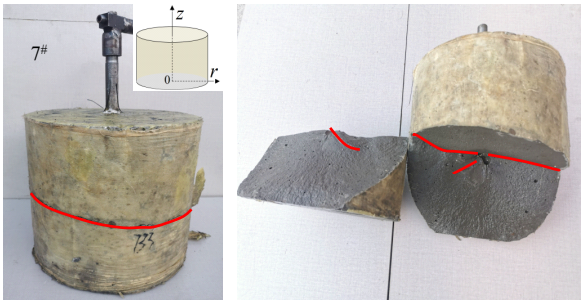

(i) Fracture surface morphology of specimen #7

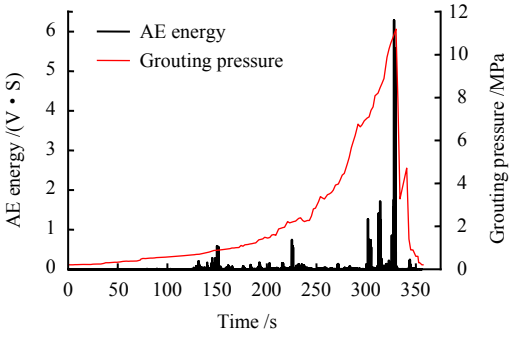

(j) AE energy and grouting pressure of specimen #7

Fig. 7 Fracture surface morphology and corresponding diagram of AE energy and grouting pressure of specimens #3 to #7 after fracturing

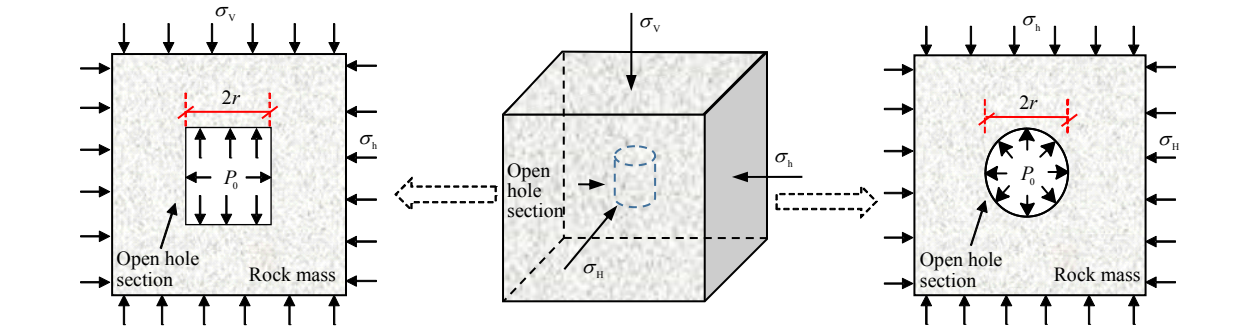

(a) Forces on the longitudinal section of open hole section (b) 3D forces on the open hole section (c) Forces on the cross-section of open hole section

Fig. 8 Forces on the open hole section

$$\left.\begin{aligned}
\sigma_\rho &= \left(\frac{\sigma_H-\sigma_h}{2}\right)\left(1+\frac{3r^4}{\rho^4}-\frac{4r^2}{\rho^2}\right)\cos 2\theta + \\
&\quad \left(\frac{\sigma_H+\sigma_h}{2}\right)\left(1-\frac{r^2}{\rho^2}\right)+\frac{r^2}{\rho^2}P_0 \\
\sigma_\theta &= -\left(\frac{\sigma_H-\sigma_h}{2}\right)\left(1+\frac{3r^4}{\rho^4}\right)\cos 2\theta + \\
&\quad \left(\frac{\sigma_H+\sigma_h}{2}\right)\left(1+\frac{r^2}{\rho^2}\right)-\frac{r^2}{\rho^2}P_0 \\
\tau_{r\theta} &= -\left(\frac{\sigma_H-\sigma_h}{2}\right)\left(1+\frac{2r^2}{\rho^2}-\frac{3r^2}{\rho^2}\right)\sin 2\theta
\end{aligned}\right\} \quad (7)$$

where r is the radius of the open hole; ρ is the radial distance from the outer wall of the open hole section; and θ is the circumferential angle.

According to the maximum tensile stress failure criterion, brittle tensile fracture occurs when the tangential stress reaches the rock tensile strength, i.e. the fracturing condition is $\sigma_\theta = \sigma_t$. According to Eq. (7), σ_θ varies with circumferential angle θ. When θ ranges between 0 and π, σ_θ takes the maximum value, thus the open hole section fails in the direction perpendicular to the minor horizontal principal stress, and the grouting pressure is equal to the fracture pressure:

$$P = 3\sigma_h - \sigma_H + \sigma_t \quad (8)$$

In this scenario, the grouting pressure within the open hole section counteracts the effect of the outer rock load and the fracture toughness of the rock itself, resulting in longitudinal fracture initiation.

Figure 9 plots the pressure-time curves of specimens #1−#7 during fracture grouting. The pressure curves of the specimens in the chamber and outside the chamber are significantly different, and the pressure curves recorded under different stress states also vary considerably. This is because the fracturing of the specimens not only counteracts their own tensile strengths, but also resists the external loads.

Without external confining pressure and axial pressure, specimens #1 and #2 crack along the transverse direction. Therefore, according to Eq. (6), the fracture initiation pressure without external confining pressure and axial pressure is

$$P_0 = \sigma_t \quad (9)$$

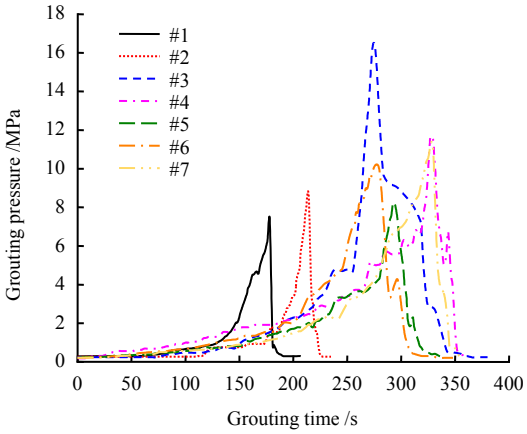

Fig. 9 Grouting pressure−time curves of specimens #1−#7

For specimens #3−#7, the axial direction of the open hole section is parallel to the axial pressure and perpendicular to the confining pressure, and the axial pressure is larger than the confining pressure, which conforms to the longitudinal crack initiation model. As $\sigma_H = \sigma_h$, according to Eq. (8), the fracture initiation pressure is simplified to

$$P_0 = 2\sigma_H + \sigma_t \quad (10)$$

The calculated fracture initiation pressures of specimens #1−#7 according to Eqs. (9) and (10) are tabulated in Table 5.

Table 5 Results of fracture grouting test for specimens #1−#7

Specimen No.	#1	#2	#3	#4	#5	#6	#7
P_0 /MPa	6.75	8.92	16.29	11.93	8.31	11.18	10.51
P_0^* /MPa	2.58	3.13	12.58	8.58	4.58	8.58	6.58

Note: P_0^* is the measured fracture initiation pressure; and P_0 is the theoretical fracture initiation pressure.

By comparing the grouting initiation pressures of specimens #1−#7 in Table 5, it is found that the

theoretical values are far less than the test values. The possible reason is that the tensile strength of rock measured by fracture grouting method is based on the theory of elasticity, in which process the specimens are in the tensile state, the direction of stress is perpendicular to the direction of concentrated stress, and thus the center of the specimen is broken first. Slurry fracturing method, however, assumes that the load at the time of specimen failure indicates that the weakest part has reached the bearing limit, which is still in the category of tensile failure[25]. Therefore, the tensile strength measured by the fracture grouting method cannot truly reflect the rock tensile strength, and may be lower than the actual value, resulting in a large gap between the theoretical grouting initiation pressure and the test results. The tensile strengths of sandy mudstone under fracture grouting deduced from the test results are listed in Table 6.

Table 6 Comparison of tensile strengths with two methods

Specimen No.	P_0^* /MPa	σ_t^* /MPa	P_0 /MPa	σ_t /MPa	σ_t^*/σ_t
#1	6.75	6.75	2.58	2.58	2.62
#2	8.92	8.92	3.13	3.13	2.85
#3	16.29	6.29	12.58	2.58	2.44
#4	11.93	5.93	8.58	2.58	2.30
#5	8.31	6.31	4.58	2.58	2.45
#6	11.18	5.18	8.58	2.58	2.01
#7	10.51	4.51	6.58	2.58	1.75

Note: σ_t^* is the tensile strength under the condition of internal pore pressure fracturing.

According to the statistics in Table 6, the tensile strengths of sandy mudstone measured by fracture grouting method σ_t^* are approximately 2.5 times the uniaxial tensile strengths σ_t. To further examine the correctness of this conclusion, the laboratory test results documented by Wu et al.[10] and Zou et al.[26] are used for verification.

According to the results in Table 7, under fracture grouting, the tensile strength of granite is 2.58 times the uniaxial tensile strength, while the tensile strength of shale is 2.42 times the uniaxial tensile strength. It follows from the above that under the condition of triaxial pore pressure, the tensile strength of rock determined by the fracture grouting method is obviously high, approximately 2.5 times the uniaxial tensile strength.

Table 7 Comparison of two tensile strengths of different rocks

Rock type	σ_H /MPa	σ_h /MPa	P_0^* /MPa	σ_t^* /MPa	P_0 /MPa	σ_t /MPa	σ_t^*/σ_t
Granite[10]	10	10	33.67	6.75	25.30	5.30	2.58
Shale[26]	15	10	20.80	6.29	17.40	2.40	2.42

5 Conclusions

(1) The good consistency between AE energy and grouting pressure curves verifies that AE is an effective means for fracture propagation detection. The strength of the specimen is positively correlated with the fracture initiation pressure; the higher the strength is, the more complex the fracturing path is.

(2) Fracture initiation pressure is more sensitive to the confining pressure than the axial pressure. When the axial pressure is constant, with the decrease in confining pressure, the constraining forces decrease, and the resistance to be overcome for fracture initiation from open hole section decreases, thus the initiation pressure decreases accordingly. When the confining pressure is constant, the axial pressure decreases and the fracture initiation pressure does not change significantly.

(3) $\Delta\sigma = \sigma_V - \sigma_H$ is defined as the stress difference. The larger the stress difference is, the more regular and smooth the fracture morphology is, and the greater the vertical degree between the direction of fracture initiation and the direction of the minor principal stress is. The smaller the stress difference is, the more irregular the fracture morphology and strike are.

(4) Under the condition of triaxial pore pressure, the tensile strength of rock determined by fracture grouting method in the open hole section is much greater, about 2.5 times the uniaxial tensile strength.

References

[1] CHENG Hua, PENG Shi-long, RONG Chuan-xin, et al. Numerical simulation and engineering application of grouting reinforcement for surrounding rocks of chamber in deep of 1 000 m by L-shaped boreholes[J]. Rock and Soil Mechanics, 2018, 39(Suppl. 2): 281−291.

[2] ZHANG Hua-lei, TU Min, CHENG Hua, et al. Breaking mechanism of overlying strata under thick unconsolidated layers and integrated grouting reinforcement technology for wind oxidation zone[J]. Journal of China Coal Society, 2018, 43(8): 40−46.

[3] CHENG Hua, LIU Xiang-yang, RONG Chuan-xin, et al. Numerical simulation and application of seepage regularity of ground grouting in deep vertical shaft [J]. Journal of Anhui University of Science and Technology (Natural Science), 2018, 38(1): 8−14.

[4] LIU Xiang-yang, CHENG Hua, LIN Jian, et al. Study of the mechanism of fracture grouting in deeply buried rock strata based on Bingham fluid slurry[J]. Advances in Civil Engineering, 2019, 2019: 1−10.

[5] CHENG Hua, LIU Xiang-yang, LIN Jian, et al. Study on

fracturing and diffusion mechanism of nonslab fracturing grouting[J]. Geofluids, 2020, 2020: 1−9.

[6] LIU Xiang-yang, CHENG Hua, LI Ming-jing, et al. Theoretical research on longitudinal fracture grouting of deep buried strata based on slurry rheology[J]. Rock and Soil Mechanics, 2021, 42(5): 1373−1380.

[7] HUANG Rong-zun. Initiation and propagation of hydraulic fracturing fractures[J]. Petroleum Exploration and Development, 1981, 7(5): 62−74.

[8] CHEN Mian, CHEN Zhi-xi, HUANG Rong-zun. Hydraulic fracturing of highly deviated wells[J]. Journal of the University of Petroleum (Edition of Natural Science), 1995, 19(2): 30−35.

[9] HUBBERT M K, WILLIS D G. Mechanics of hydraulic fracturing[J]. Transactions of Society of Petroleum Engineers of AIME, 1957, 210: 153−168.

[10] WU Jing-nong, WU Mian-ba. Experimental research of rock fracture under pore-triaxial stress condition[J]. Seismology and Geology, 1986, 8(2): 69−76.

[11] YUN J W, PARK J J, KWON Y S, et al. Cement-based fracture grouting phenomenon of weathered granite soil[J]. KSCE Journal of Civil Engineering, 2017, 21(1): 232−242.

[12] FISHER M K, WARPINSKI N R. Hydraulic fracture height growth: real data[J]. SPE Production & Operations, 2012, 27(1): 8−19.

[13] ALFARO M C, WONG R C. Laboratory studies on fracturing of low-permeability soils[J]. Canadian Geotechnical Journal, 2001, 38(2): 303−315.

[14] LIN Hai-xiao, DU Chun-zhi. Experimental research on the quasi three-axis hydraulic fracturing of coal[J]. Journal of China Coal Society, 2011, 36(11): 1801−1805.

[15] ZHOU Rui-he, CHENG Hua, CAI Hai-bing, et al. Dynamic characteristics and damage constitutive model of mudstone under impact loading[J]. Materials, 2022, 15(3): 1128.

[16] WANG Han-peng, LI Shu-cai, ZHANG Qiang-yong, et al. Development of a new geomechanical similar material[J]. Chinese Journal of Rock Mechanics and Engineering, 2006, 25(9): 1842−1847.

[17] LI Shu-chen, FENG Xian-da, LI Shu-cai, et al. Research and development of a new similar material for solid-fluid coupling and its application[J]. Chinese Journal of Rock Mechanics and Engineering, 2010, 29(2): 281−288.

[18] HUANG Yan-hua, YANG Sheng-qi, LIU Xiang-ru. Experimental and numerical study on the mechanical characteristics of rock-like materials[J]. Journal of Experimental Mechanics, 2014, 29(2): 239−249.

[19] LIU Xiang-yang. The mechanism of capillary-film water migration in freezing soil and its experimental study[D]. Hefei: Hefei University of Technology, 2021.

[20] DENG Hua-feng, ZHU Min, LI Jian-lin, et al. Study of mode-I fracture toughness and its correlation with strength parameters of sandstone[J]. Rock and Soil Mechanics, 2012, 33(12): 3585−3591.

[21] XUE Wei-pei, YAO Zhi-shu, WANG Xiao-jian, et al. Research on strength criterion and bearing capacity of shaft lining concrete under axial pressure and hydraulic pressure[J]. China Safety Science Journal, 2018, 28(8): 129−134.

[22] LI Peng, MIAO Sheng-jun. Analysis of characteristics of in-situ stress field and fault activity in coal mining area in China[J]. Journal of China Coal Society, 2016, 41(Suppl. 2): 319−329.

[23] XU Jia-lin, CHEN Jia-xuan, JIANG Kun. Effect of load transfer of unconsolidated confined aquifer on compound breakage of key strata[J]. Chinese Journal of Rock Mechanics and Engineering, 2007, 26(4): 699−704.

[24] CHENG Liang, LU Yi-yu, GE Zhao-long, et al. Initiation pressure calculation model and judgment criterion for hydraulic fracturing of inclined coal seam[J]. Rock and Soil Mechanics, 2015, 29(2): 444−450.

[25] YOU Ming-qing, SU Cheng-dong. Study of strength and failure of hollow cylinders and rings of sandstone under compression-tension stresses[J]. Chinese Journal of Rock Mechanics and Engineering, 2010, 29(6): 1096−1105.

[26] ZOU Yushi, MA Xinfang, ZHOU Tong, et al. Hydraulic fracture growth in a layered formation based on fracturing experiments and discrete element modeling[J]. Rock Mechanics and Rock Engineering, 2017, 50: 2381−2395.